CrossMark

Optical and magnetic properties of Mg-doped $ZnFe_2O_4$ nanoparticles prepared by rapid microwave combustion method

A. Manikandan [a], J. Judith Vijaya [a,*], M. Sundararajan [b], C. Meganathan [a], L. John Kennedy [b], M. Bououdina [c,d]

[a] Catalysis and Nanomaterials Research Laboratory, Department of Chemistry, Loyola College, Chennai 600 034, India
[b] Materials Division, School of Advanced Sciences, Vellore Institute of Technology University Chennai Campus, Chennai 600 127, India
[c] Department of Physics, College of Science, University of Bahrain, PO Box 32038, Bahrain
[d] Nanotechnology Centre, University of Bahrain, PO Box 32038, Bahrain

ARTICLE INFO

ABSTRACT

Mg-doped $ZnFe_2O_4$ samples were prepared by a microwave combustion method. The obtained samples were characterized by powder X-ray diffraction (XRD), high resolution scanning electron microscopy (HR-SEM), energy dispersive X-ray analysis, UV–Visible diffuse reflectance spectra (DRS), photoluminescence (PL) spectra and vibrating sample magnetometer (VSM). XRD results confirm the formation of cubic spinel-type structure with an average crystallite size in the range of 15–43 nm. Lattice parameter decreases with increasing Mg concentration, due to the smaller ionic radius of Mg^{2+} ion. The HR-SEM images show the morphology of the samples as spherical shaped particles in agglomeration. The broad visible emission band is observed in the entire PL spectrum. The estimated band gap energy is found to decrease with increasing Mg content (2.15–1.42 eV). The magnetization showed an increasing trend with increasing Mg concentration ($x = 0.5$), due to the rearrangement of cations at tetrahedral and octahedral sites.

© 2013 The Authors. Published by Elsevier Ltd.
Open access under CC BY-NC-ND license.

* Corresponding author. Tel.: +91 44 28178200; fax: +91 44 28175566.
  E-mail address: jjvijayaloyola@yahoo.co.in (J. Judith Vijaya).

1. Introduction

Nanocrystalline spinel ferrites are the important class of materials having a variety of electronic, magnetic and catalytic properties. The ferrite nanoparticles are having large number of applications in different areas such as biomedical, ferrofluid, magnetic media, microwave, magnetocaloric refrigeration and gas sensors [1–8]. The ferrites are semiconductor materials with the formula MFe_2O_4, where *M* can be a divalent metal cation [9].

Zinc ferrite ($ZnFe_2O_4$) is a normal spinel structure, where Zn^{2+} cations occupy tetrahedral sites [10]. They are chemically and thermally stable semiconductor materials suitable for a wide variety of applications including magnetic materials, catalysts, photocatalysts, magnetic resonance imaging (MRI), drug delivery and pigments [11–13]. Recently, the nanoscale $ZnFe_2O_4$ has been extensively studied by worldwide researchers, because of their unique size dependent physical and chemical properties as compared to the bulk counterpart materials.

Several preparation techniques for $ZnFe_2O_4$ nanoparticles with uniform size have been developed including co-precipitation, sonochemical emulsification, evaporation, sol–gel, hydrothermal, mechanical milling, combustion method and reverse micelle technique [14–20]. However, in most of the above cases, they require handling of large amounts of chemicals with long reaction time and low yield, which usually make the process expensive as well as it pollutes the environment by the release of toxic gases, and therefore, they are not suitable for large-scale industrial applications [21].

However, microwave combustion synthesis of nanomaterials is gaining much interest among researchers, due to its unique features such as environment friendly method, short reaction time, rapid heating, energy saving, and high reaction rate. During the microwave reaction, microwave energy transforms into heat inside the material, which reduces the energy consumption, decreases the reaction processing time and provides rapid, controllable and homogeneous volumetric heating to produce the final products within few minutes [21–25].

This paper reports the effect of Mg-doping on structural, optical and magnetic properties of $Zn_{1-x}Mg_xFe_2O_4$ (*x* = 0.0, 0.1, 0.2, 0.3 0.4, 0.5, 0.6, 0.7 and 0.8) nanoferrite particles prepared by microwave combustion method. Various characterization techniques have been carried out using X-ray diffraction (XRD), high resolution scanning electron microscopy (HR-SEM), energy dispersive X-ray spectroscopy (EDX), UV–Visible diffuse reflectance spectra (DRS), photoluminescence (PL) spectra, vibrating sample magnetometer (VSM) techniques and the results are presented herein.

2. Experimental

2.1. Materials and methods

All the chemicals used in this study were of analytical grade obtained from Merck, India and were used as received without further purification. Zinc nitrate ($Zn(NO_3)_2 \cdot 6H_2O$, 98%), ferric nitrate ($Fe(NO_3)_3 \cdot 9H_2O$, 98%) and magnesium nitrate ($Mg(NO_3)_2 \cdot 6H_2O$) were used as precursors and urea as a fuel for this reaction. The compositions were prepared with the addition of magnesium of different molar ratios ($Zn_{1-x}Mg_xFe_2O_4$ with *x* = 0.0, 0.1, 0.2, 0.3 0.4, 0.5, 0.6, 0.7 and 0.8) to $ZnFe_2O_4$. For the preparation of pure zinc ferrite using the microwave combustion technique, the precursor mixture in urea was placed into a domestic microwave oven and exposed to the microwave energy in a 2.45 GHz multimode cavity at 750 W for 10 min. After the completion of the reaction, the solid powder was obtained and then it was washed with ethanol and dried at 70 °C for 1 h. The as-prepared samples, $Zn_{1-x}Mg_xFe_2O_4$ with *x* = 0.0, 0.1, 0.2, 0.3 0.4, 0.5, 0.6, 0.7 and 0.8, were labeled as $ZnFe_2O_4$, $Zn_{0.9}Mg_{0.1}Fe_2O_4$, $Zn_{0.8}Mg_{0.2}Fe_2O_4$, $Zn_{0.7}Mg_{0.3}Fe_2O_4$, $Zn_{0.6}Mg_{0.4}Fe_2O_4$, $Zn_{0.5}Mg_{0.5}Fe_2O_4$, $Zn_{0.4}Mg_{0.6}Fe_2O_4$, $Zn_{0.3}Mg_{0.7}Fe_2O_4$ and $Zn_{0.2}Mg_{0.8}Fe_2O_4$ respectively.

The entire microwave combustion process produce zinc ferrite powders in a microwave-oven operated at a power of 750 W has produced $ZnFe_2O_4$ within 10 min. The proposed combustion reaction may be as follows:

$$2Zn(NO_3)_2 \cdot 6H_2O_{(S)} + 4Fe(NO_3)_3 \cdot 9H_2O_{(S)} + 4CO(NH_2)_{2(S)} + 2O_{2(g)} \rightarrow 2ZnFe_2O_{4(S)} + 56H_2O_{(g)} \uparrow$$

$$+ 4CO_{2(g)} \uparrow + 4N_{2(g)} \uparrow + 16NO_{2(g)} \uparrow$$
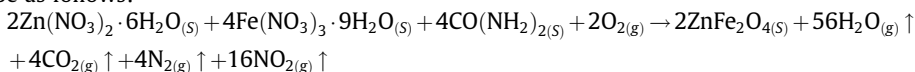
2.2. Characterizations

The structural characterization of Mg-doped $ZnFe_2O_4$ ($Zn_{1-x}Mg_xFe_2O_4$ with x = 0.0, 0.1, 0.2, 0.3 0.4, 0.5, 0.6, 0.7 and 0.8) nanoparticles were performed using Rigaku Ultima X-ray diffractometer equipped with Cu Kα radiation (λ = 1.5418 Å). Structural refinements using the Rietveld method was carried out by PDXL program; both refined lattice parameters and crystallite size of the obtained ferrites were reported. Morphological studies and energy dispersive X-ray analysis (EDX) of pure and Mg-doped $ZnFe_2O_4$ nanoparticles have been performed with a Jeol JSM6360 high resolution scanning electron microscope (HR-SEM). The UV–Visible diffuse reflectance spectrum (DRS) was recorded using Cary100 UV–Visible spectrophotometer to estimate their band gap energy. The photoluminescence (PL) properties were recorded using Varian Cary Eclipse Fluorescence Spectrophotometer. Magnetic measurements were carried out at room temperature using a PMC MicroMag 3900 model vibrating sample magnetometer (VSM) equipped with 1 Tesla magnet.

3. Results and discussion

3.1. X-ray diffraction (XRD) analysis

The structure and phase purity of the samples were confirmed by analyzing the X-ray powder diffraction patterns. Fig. 1a–i, shows the XRD patterns of $Zn_{1-x}Mg_xFe_2O_4$ samples prepared with various Mg substitutions (x = 0.0, 0.1, 0.2, 0.3 0.4, 0.5, 0.6, 0.7 and 0.8). All the observed reflections could be assigned to cubic spinel lattice indicating their single phase structure with no traces of other impurity phases (e.g. Fe_2O_3, ZnO etc.). The peaks could be indexed as (2 2 0), (3 1 1), (4 0 0), (4 2 2), (5 1 1), (4 4 0) and (5 3 3), which are characteristics of single-phase cubic spinel structure (JCPDS card no. 22-1012). There is no additional peak for all compositions, which indicates that all the samples crystallize in single-phase cubic structure [26].

The average crystallite size of the samples is calculated from the diffraction peak of the (3 1 1) plane in the XRD profile, in accordance with Debye–Scherrer formula [21]:
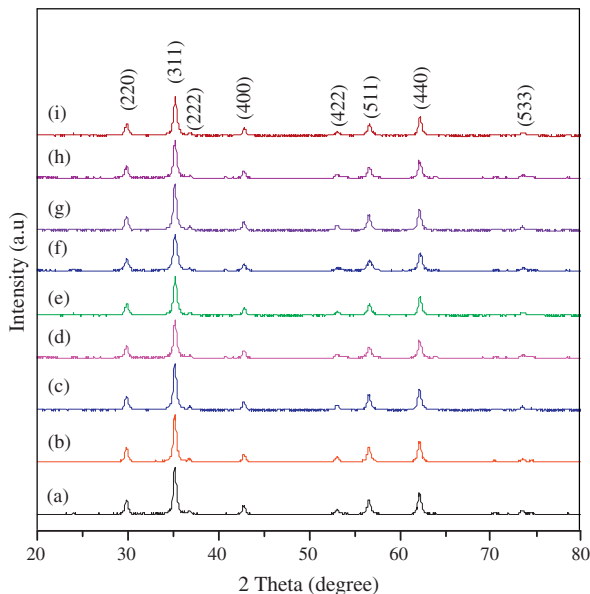
Fig. 1. (a–i) XRD patterns of (a) $ZnFe_2O_4$, (b) $Zn_{0.9}Mg_{0.1}Fe_2O_4$, (c) $Zn_{0.8}Mg_{0.2}Fe_2O_4$, (d) $Zn_{0.7}Mg_{0.3}Fe_2O_4$, (e) $Zn_{0.6}Mg_{0.4}Fe_2O_4$, (f) $Zn_{0.5}Mg_{0.5}Fe_2O_4$, (g) $Zn_{0.4}Mg_{0.6}Fe_2O_4$, (h) $Zn_{0.3}Mg_{0.7}Fe_2O_4$, and (i) $Zn_{0.2}Mg_{0.8}Fe_2O_4$ samples.

Table 1
Lattice parameter, crystallite size (Scherrer formula, Rietveld analysis) and band gap values of $Zn_{1-x}Mg_xFe_2O_4$ (x = 0.0, 0.1, 0.2, 0.3, 0.4, 0.5, 0.6, 0.7 and 0.8) system.

Samples	Lattice parameter (Å) Rietveld analysis	Crystallite size D (nm)		Band gap (eV)	Strain (%)	S (Goodness of fit)
		Scherrer formula	Rietveld analysis			
$ZnFe_2O_4$	8.443	41.20	43	2.15	0.067	1.184
$Zn_{0.9}Mg_{0.1}Fe_2O_4$	8.441	39.35	41	2.01	0.066	1.137
$Zn_{0.8}Mg_{0.2}Fe_2O_4$	8.439	36.78	39	1.98	0.063	1.092
$Zn_{0.7}Mg_{0.3}Fe_2O_4$	8.435	31.59	37	1.96	0.060	1.102
$Zn_{0.6}Mg_{0.4}Fe_2O_4$	8.433	26.53	29	1.80	0.058	1.107
$Zn_{0.5}Mg_{0.5}Fe_2O_4$	8.431	19.59	21	1.75	0.055	1.105
$Zn_{0.4}Mg_{0.6}Fe_2O_4$	8.430	17.92	19	1.68	0.053	1.103
$Zn_{0.3}Mg_{0.7}Fe_2O_4$	8.429	16.28	17	1.55	0.050	1.101
$Zn_{0.2}Mg_{0.8}Fe_2O_4$	8.427	15.87	16	1.42	0.047	1.105

$$L = \frac{0.89\lambda}{\beta \cos\theta}$$

where L is the average particle, λ, the X-ray wavelength (0.1542 nm), β, full width at half maximum (FWHM) and θ, the Bragg angle of the (3 1 1) plane. The crystallite size of the samples was summarized in Table 1. It has been observed that the crystallite size is decreased from 41.20–15.87 nm with increase in Mg content [27]. It has a minimum crystallite size of 15.87 nm for 0.8 Mg concentration, due to the smaller ionic radius of Mg^{2+} ions. Similar results were found by Rahman et al. [9].

In order to further analyze the structural change, the measured XRD patterns of the samples were simulated based on the Rietveld refinement method. Rietveld XRD data analysis for the samples is shown in Fig. 2a–i. It was designed to refine simultaneously both the structural and microstructural parameters. During the refinements, the goodness of fit is defined by the reliability factor $S = R_{wp}/R_e$, where R_{wp} and R_e, are, respectively, the R-weighted and the R-expected patterns. The obtained values of the lattice parameter and crystallite sizes from the Rietveld analysis are shown in Fig. 3 and Table 1. The lattice parameter of pure $ZnFe_2O_4$ is found to be equal to 8.443 Å, which is in good accordance with the standard value of 8.441 Å (JCPDS No. 22-1012). The lattice parameter decreases with increasing Mg content from 8.443 to 8.427 Å, thus obeying Vegard's law [28]. The Vegard's law is based on the change due to ionic radii of replacing and replaced ions and predicts the linear change in the lattice parameter for the spinel system with the substitution of different ions. The ionic radius of Mg^{2+} ion (0.65 Å) is smaller than that of Zn^{2+} ion (0.83 Å), and thus causes an effective decrease in the lattice constant. Similar results were reported earlier by Rahman et al. [9] and Salah et al. [27]. A linear decrease in the lattice spacing thus indicates that the Mg ions are replacing the Zn ions in Zn ferrite matrix [24,28]. This explains the decrease of lattice constant with Mg doping and also confirms that Mg is occupied in the lattice of spinel ferrite [29].

The thermodynamic solubility of the Mg-doped $ZnFe_2O_4$ system has attracted much interest. The spinel solid solutions of Mg-doped $ZnFe_2O_4$ were prepared by a microwave heating using a nitrate mixture of Zn, Fe, and Mg in the required ratio with urea as a fuel. During the microwave combustion, the temperature increases up to 400 °C [30]. The ionic radius of Mg^{2+} is 0.65 Å, which is lower than Zn^{2+} radius (0.83 Å); and thereby it can be easily soluble within $ZnFe_2O_4$ and produces solid solutions. The formation of solid solutions was confirmed by X-ray diffraction analysis. Mg-doped zinc ferrite is a spinel-type crystal and the solid solutions are considered to be the products of mixing of Mg in $ZnFe_2O_4$. It is well known that the thermodynamic solubility of the spinel solid solutions is connected with the cation distribution [31]. On the other hand, cation distribution is closely related to their magnetic properties. Thus, the choice of a proper composition of solid solutions will have a better control of the magnetic properties of these materials, which are of interest for the electronic industry. From metallurgical point of view, the formation of zinc ferrite during microwave heating is one of the major
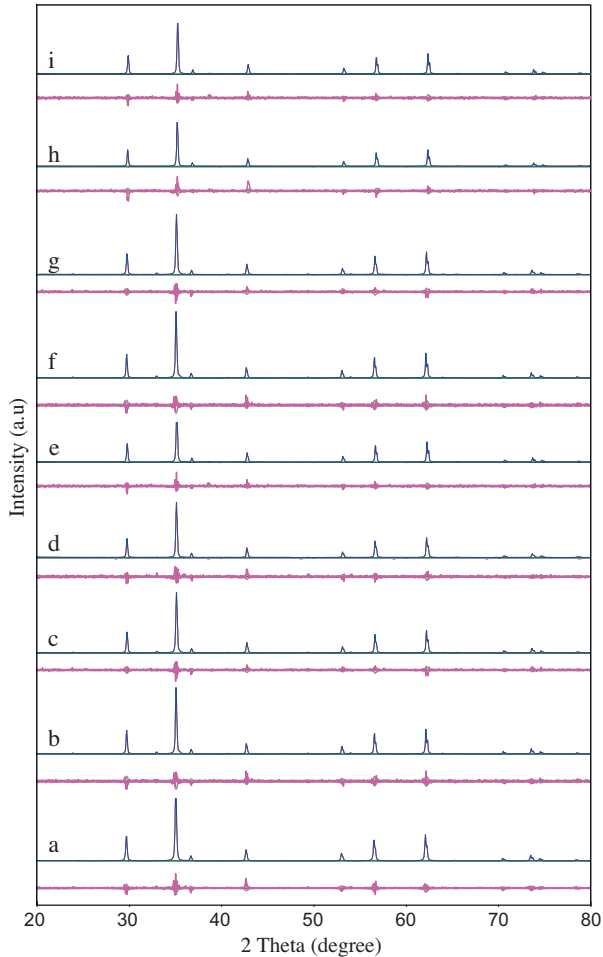
Fig. 2. (a–i) XRD pattern refinements using the Rietveld method of (a) $ZnFe_2O_4$, (b) $Zn_{0.9}Mg_{0.1}Fe_2O_4$, (c) $Zn_{0.8}Mg_{0.2}Fe_2O_4$, (d) $Zn_{0.7}Mg_{0.3}Fe_2O_4$, (e) $Zn_{0.6}Mg_{0.4}Fe_2O_4$, (f) $Zn_{0.5}Mg_{0.5}Fe_2O_4$, (g) $Zn_{0.4}Mg_{0.6}Fe_2O_4$, (h) $Zn_{0.3}Mg_{0.7}Fe_2O_4$, and (i) $Zn_{0.2}Mg_{0.8}Fe_2O_4$ samples (experimental data, upper solid line: calculated pattern, lower solid line: intensity difference).

obstacles, solubilising Mg in $ZnFe_2O_4$ during combustion. Therefore, acknowledge of the thermodynamic solubility of zinc ferrite and its solid solutions are desirable [32,33].

3.2. Scanning electron microscopy (SEM) studies

The morphological characteristics of the obtained $Zn_{1-x}Mg_xFe_2O_4$ (x = 0.0, 0.1, 0.2, 0.3 0.4, 0.5, 0.6, 0.7 and 0.8) nanoparticles were investigated by the high resolution scanning electron microscopy (HR-SEM) and are shown in Fig. 4. HR-SEM images of $Zn_{1-x}Mg_xFe_2O_4$ samples (Fig. 4a–i) reveal that all the samples exhibit a compact arrangement of homogeneous nanoparticles with spherical shape. Fig. 4a shows the presences of pure $ZnFe_2O_4$ nanoparticles, and Fig. 4b–i, shows the images of Mg-doped Zn ferrite nanoparticles, which are homogeneous and agglomerated with diameter ranging from 40 to 43 nm for undoped and 35–15 nm for Mg-doped $ZnFe_2O_4$ samples. Nanoparticles are agglomerated due to the presence of magnetic interactions among the particles [9].
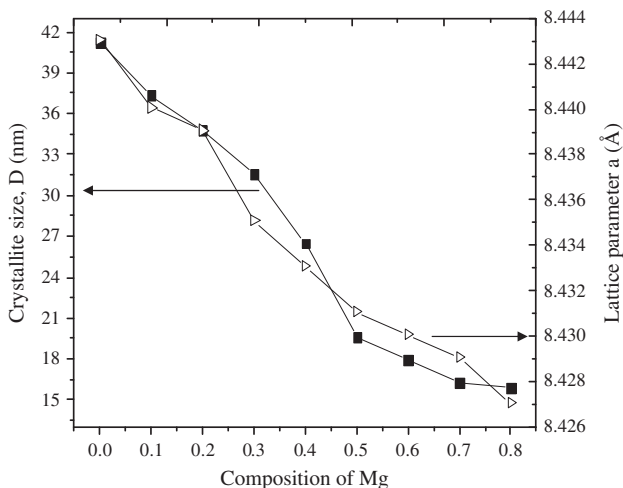
Fig. 3. Evolution of the lattice parameter and crystallite size of $Zn_{1-x}Mg_xFe_2O_4$ (x = 0.0, 0.1, 0.2, 0.3, 0.4, 0.5, 0.6, 0.7 and 0.8) system.

3.3. Energy dispersive X-ray (EDX) analysis

EDX spectra of pure and magnesium doped zinc ferrites, $Zn_{1-x}Mg_xFe_2O_4$ system (x = 0.0, 0.1, 0.2, 0.3 0.4, 0.5, 0.6, 0.7 and 0.8) are shown in Fig. 5a–i. Fig. 5a shows the peaks of Fe, Zn and O elements in pure $ZnFe_2O_4$ and Fig. 5b–i, shows the peaks of Fe, Zn, Mg and O elements for Mg-doped $ZnFe_2O_4$ samples. The observed percentage of Mg/Zn value matches well with the amount of Mg/Zn used in the respective precursors (inset of Fig. 5a–i). It is interesting to note that the preparation condition completely favors the formation of mixed ferrites and allow us to study the effect of increasing Mg content on the properties of the zinc ferrite. The above mentioned results confirm the formation of pure and Mg-doped $ZnFe_2O_4$ phase.

3.4. Diffuse reflectance spectroscopy (DRS) studies

To study the effect of crystallite size on the optical properties of $ZnFe_2O_4$ semiconductor ferrite materials, the UV–Visible diffuse reflectance measurement was carried out. The band gap energy can be approximately calculated from the optical reflectance data by the Kubelka–Munk function, $F(R) = (1 - R)^2/2R$, where R is the diffuse reflectance [21,34]. A graph is plotted between $[F(R)h\upsilon]^2$ and $h\upsilon$, and the intercept obtained is the band gap energy (Fig. 6a–i). The estimated values of the band gap of $Zn_{1-x}Mg_xFe_2O_4$ (x = 0.0, 0.1, 0.2, 0.3 0.4, 0.5, 0.6, 0.7 and 0.8) nanoparticles are 2.15, 2.01, 1.98, 1.96, 1.80, 1.75, 1.68, 1.55 and 1.42 eV, respectively (Fig. 7 and Table 1). It clearly shows that there is a decrease in the band gap of the Mg-doped $ZnFe_2O_4$ samples, when compared to the pure $ZnFe_2O_4$. The band-gap (E_g) value of bulk $ZnFe_2O_4$ is 1.9 eV, and hence there is a blue shift for $ZnFe_2O_4$, $Zn_{0.9}Mg_{0.1}Fe_2O_4$, $Zn_{0.8}Mg_{0.2}Fe_2O_4$, $Zn_{0.7}Mg_{0.3}Fe_2O_4$ and red shift for $Zn_{0.6}Mg_{0.4}Fe_2O_4$, $Zn_{0.5}Mg_{0.5}Fe_2O_4$, $Zn_{0.4}Mg_{0.6}Fe_2O_4$, $Zn_{0.3}Mg_{0.7}Fe_2O_4$ and $Zn_{0.2}Mg_{0.8}Fe_2O_4$ samples. This may be due to the additional sub-band-gap energy levels that are induced by the abundant surface and interface defects in the agglomerated nanoparticles [35,36]. The shift in E_g of the $Zn_{1-x}Mg_xFe_2O_4$ nanoparticles with the decreasing crystallite size is the result of quantum confinement effects arising from the small size regime [37,38].

3.5. Photoluminescence (PL) studies

In order to study the defects and other impurity states of the system, photoluminescence (PL) spectra of the Mg-doped $ZnFe_2O_4$ samples were recorded. Fig. 8 shows room temperature PL spectrum of
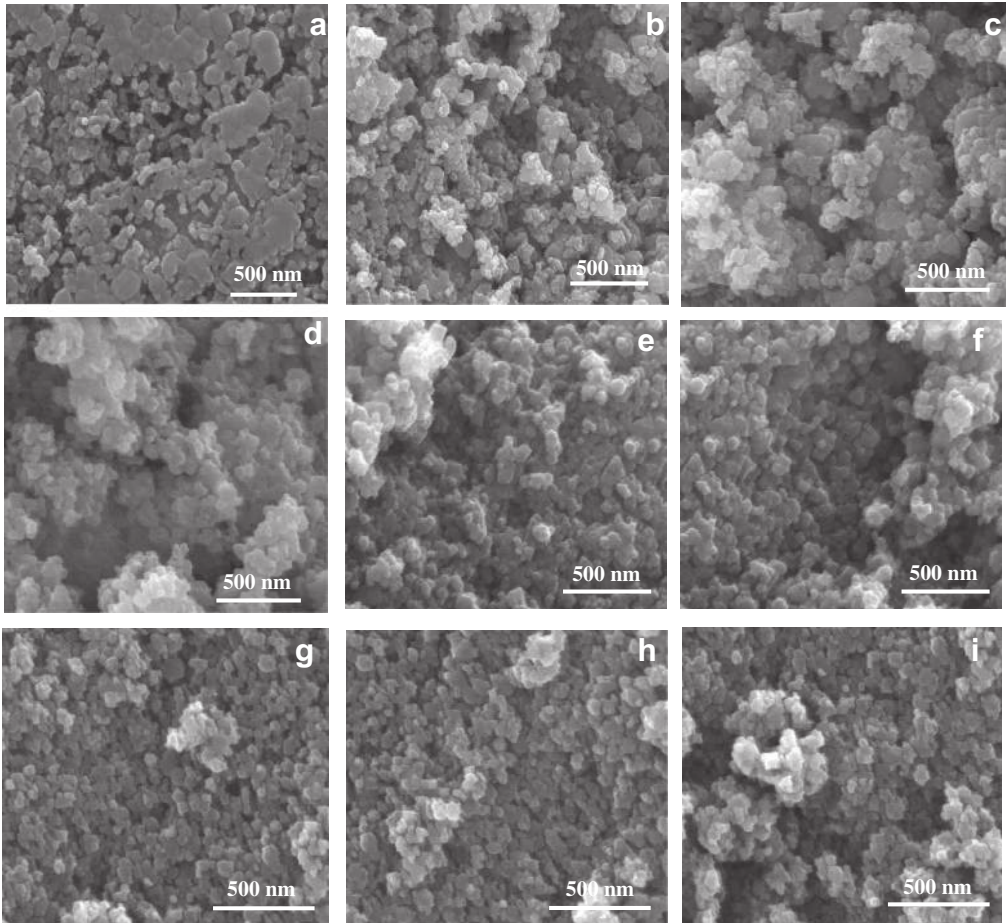
Fig. 4. (a–i) HR-SEM images of (a) $ZnFe_2O_4$, (b) $Zn_{0.9}Mg_{0.1}Fe_2O_4$, (c) $Zn_{0.8}Mg_{0.2}Fe_2O_4$, (d) $Zn_{0.7}Mg_{0.3}Fe_2O_4$, (e) $Zn_{0.6}Mg_{0.4}Fe_2O_4$, (f) $Zn_{0.5}Mg_{0.5}Fe_2O_4$, (g) $Zn_{0.4}Mg_{0.6}Fe_2O_4$, (h) $Zn_{0.3}Mg_{0.7}Fe_2O_4$, and (i) $Zn_{0.2}Mg_{0.8}Fe_2O_4$ samples.

Mg doped $ZnFe_2O_4$ system, i.e. $Zn_{1-x}Mg_xFe_2O_4$ (x = 0.0, 0.1, 0.2, 0.3 0.4, 0.5, 0.6, 0.7 and 0.8). The samples were excited by using the excitation wavelength at 414 nm. All the samples showed the characteristic near-band-edge (NBE) emission of pure and Mg-doped $ZnFe_2O_4$ at around 428 nm. A broader visible emission band was obtained for all the samples centered at 428 nm, and is attributed to the recombination of electrons deeply trapped in oxygen vacancies with photogenerated holes [39]. As we increase the doping concentration of Mg into $ZnFe_2O_4$, overall intensities of the peak for all the samples decrease. This behavior can be attributed to the appearance of new electronic levels between the conduction and the valence band and might be due to the increase in intrinsic defects [21]. Similar results were reported in other literatures, in which the values of the band gap energy given are 1.9 and 2.23 eV [40,41]. Fan et al. reported similar band gaps (2.1, 2.0 and 19 eV) for pure zinc ferrites with three different ranges of particle sizes [42].

3.6. VSM measurements

The magnetic properties of the prepared samples have been determined at room temperature using a vibrating sample magnetometer (VSM) in the applied filed ranging from −10 to +10 kOe. Hysteresis
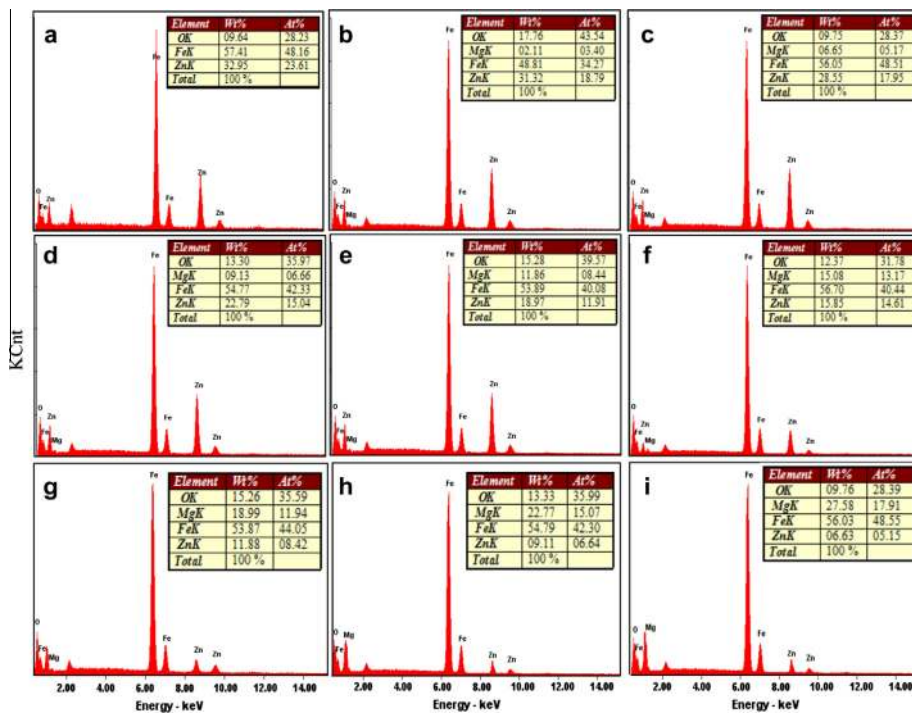
Fig. 5. (a–i) EDX spectra of (a) $ZnFe_2O_4$, (b) $Zn_{0.9}Mg_{0.1}Fe_2O_4$, (c) $Zn_{0.8}Mg_{0.2}Fe_2O_4$, (d) $Zn_{0.7}Mg_{0.3}Fe_2O_4$, (e) $Zn_{0.6}Mg_{0.4}Fe_2O_4$, (f) $Zn_{0.5}Mg_{0.5}Fe_2O_4$, (g) $Zn_{0.4}Mg_{0.6}Fe_2O_4$, (h) $Zn_{0.3}Mg_{0.7}Fe_2O_4$, and (i) $Zn_{0.2}Mg_{0.8}Fe_2O_4$ samples.

plots showing the variation of magnetization (M_s, emu/g) as a function of applied magnetic field (H, Oe) were plotted for prepared nanocrystalline $Zn_{1-x}Mg_xFe_2O_4$ (x = 0.0, 0.1, 0.2, 0.3 0.4, 0.5, 0.6, 0.7 and 0.8) powders are shown in Fig. 9. $ZnFe_2O_4$ is a soft magnetic material, and when Zn^{2+} in $ZnFe_2O_4$ is substituted by Mg^{2+} ions, there is a severe change in the magnetic properties like saturation magnetization (M_s), remanent magnetization (M_r) and coercivity (H_c) as shown in Fig. 10(a–c) [43,44]. It is observed that M_s of the $Zn_{1-x}Mg_xFe_2O_4$ nanoparticles gradually increased with the increase of Mg^{2+} content until x = 0.5, and rapidly decreased for x larger than 0.5, i.e. x = 0.6, 0.7 and 0.8 (as shown in Table 2). Hence, the M_s of $Zn_{1-x}Mg_xFe_2O_4$ nanoparticles depends on the distribution of Fe^{3+} ions among tetrahedral and octahedral lattice sites, because both Mg^{2+} and Zn^{2+} ions are non-magnetic in nature.

The samples $ZnFe_2O_4$, $Zn_{0.9}Mg_{0.1}Fe_2O_4$ and $Zn_{0.8}Mg_{0.2}Fe_2O_4$ with lesser Mg concentration (x = 0.0, 0.1 and 0.2) showed superparamagnetic behavior. This indicates that Zn^{2+} ions occupied the tetrahedral sites and Fe^{3+} ions at the octahedral sites, whereas the dopant Mg^{2+} ions occupied either octahedral or tetrahedral sites [45], thus showing superparamagnetic behavior. Similar results were reported in literature [46]. The M_s value of the samples $Zn_{0.7}Mg_{0.3}Fe_2O_4$, $Zn_{0.6}Mg_{0.4}Fe_2O_4$ and $Zn_{0.5}Mg_{0.5}Fe_2O_4$ are 25.31, 45.16 and 64.98 emu/g, respectively. There is an increase in the ferromagnetic behavior for $Zn_{0.7}Mg_{0.3}Fe_2O_4$, $Zn_{0.6}Mg_{0.4}Fe_2O_4$ and $Zn_{0.5}Mg_{0.5}Fe_2O_4$ samples with increase in Mg^{2+} concentration. The value of M_s reached a maximum value of 64.98 emu/g, the x is 0.5. Increase of the net magnetization (M_s) with increasing Mg concentration is due to the misbalance of Fe^{3+} ions in octahedral (B) and tetrahedral (A) sites, superexchange interactions and the non-collinear nature of moments in the B-site, which results in the increase of the net magnetization [47,48]. Rahman et al. [9] prepared $Zn_{1-x}Mg_xFe_2O_4$ nanoparticles by co-precipitation method and they have reported that the M_s values increase with increasing Mg content.

On further increasing the concentration of Mg in $ZnFe_2O_4$ nanocrystals, the M_s value of the samples $Zn_{0.4}Mg_{0.6}Fe_2O_4$, $Zn_{0.3}Mg_{0.7}Fe_2O_4$ and $Zn_{0.2}Mg_{0.8}Fe_2O_4$ are decreases (i.e. 58.62, 37.72 and 21.59 emu/g,
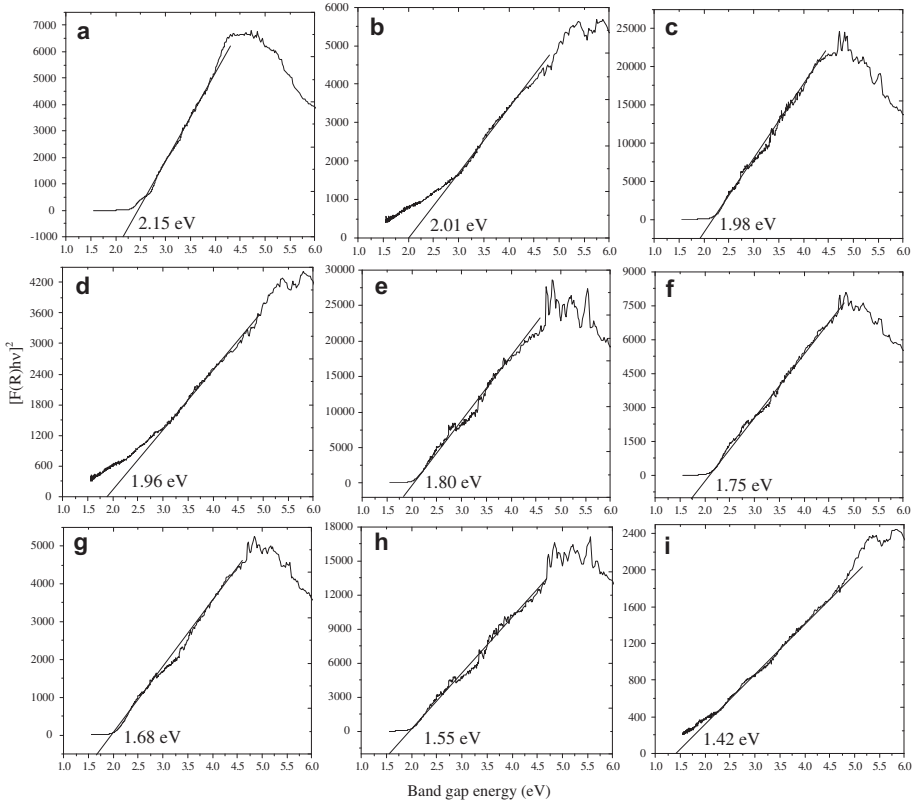
Fig. 6. (a–i) UV–Visible diffuse reflectance spectra of (a) $ZnFe_2O_4$, (b) $Zn_{0.9}Mg_{0.1}Fe_2O_4$, (c) $Zn_{0.8}Mg_{0.2}Fe_2O_4$, (d) $Zn_{0.7}Mg_{0.3}Fe_2O_4$, (e) $Zn_{0.6}Mg_{0.4}Fe_2O_4$, (f) $Zn_{0.5}Mg_{0.5}Fe_2O_4$, (g) $Zn_{0.4}Mg_{0.6}Fe_2O_4$, (h) $Zn_{0.3}Mg_{0.7}Fe_2O_4$, and (i) $Zn_{0.2}Mg_{0.8}Fe_2O_4$ samples.
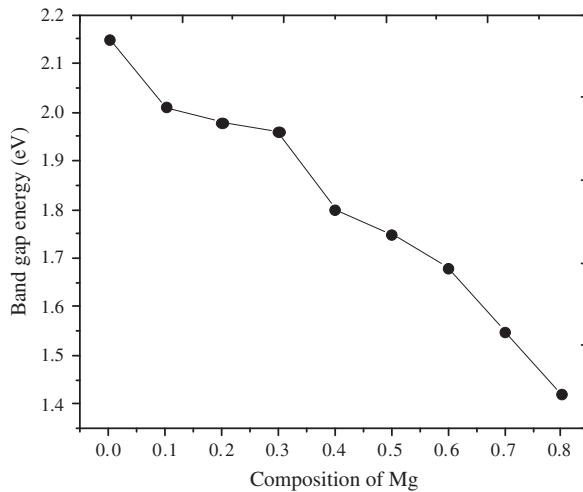
Fig. 7. Variation of the band gap energy of $Zn_{1-x}Mg_xFe_2O_4$ (x = 0.0, 0.1, 0.2, 0.3, 0.4, 0.5, 0.6, 0.7 and 0.8) system.
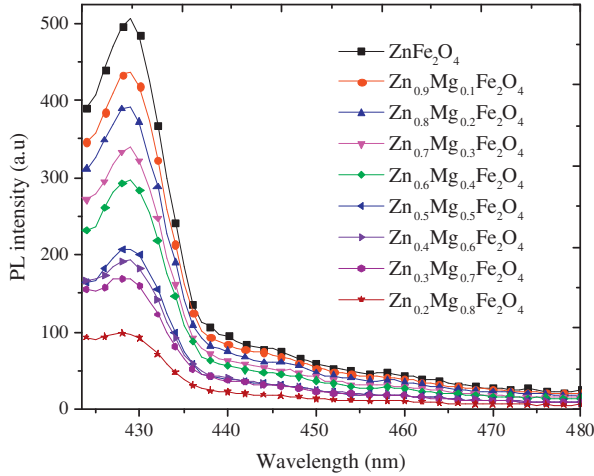
Fig. 8. Room temperature PL spectra of $Zn_{1-x}Mg_xFe_2O_4$ (x = 0.0, 0.1, 0.2, 0.3, 0.4, 0.5, 0.6, 0.7 and 0.8) system.
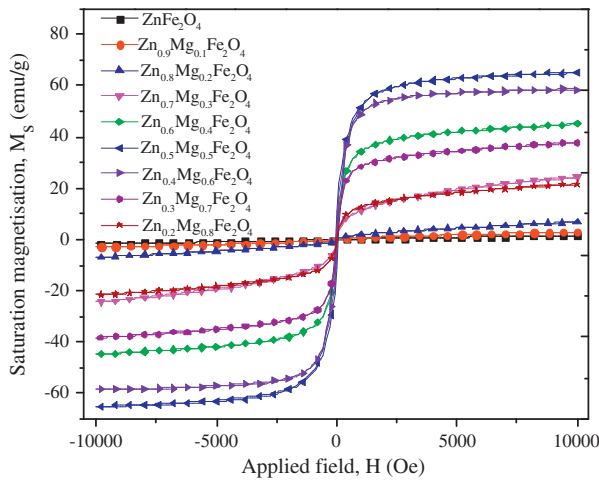
Fig. 9. Magnetic hysteresis (M–H) loops of $Zn_{1-x}Mg_xFe_2O_4$ (x = 0.0, 0.1, 0.2, 0.3, 0.4, 0.5, 0.6, 0.7 and 0.8) system.

respectively). It is due to the dopant Mg^{2+} ions, which prefers to occupy the octahedral sites may push Fe^{3+} to the A-site, which in turn decreases the value of M_s. However, the migration towards A-sites, would lead to the increase of Fe^{3+} concentration in A-sites, which gives rise to antiparallel spin coupling and spin canting, resulting in the weakening of A–B exchange coupling, and thereby decreases the net magnetic moment [49–51]. The concentration and types of cations substitution also have very dominant effect on the magnetic properties. According to the Neel's two sublattice model of ferrimagnetism [52], the magnetic moment per formula unit is expressed as,

$$M(X) = |M_{B(x)} - M_{A(x)}|$$

where, M_B and M_A are the B- and A-sublattice magnetic moment in μB respectively. Actually, the net magnetic moment determines the M_s value. Zinc ferrite is a normal spinel, non-magnetic ion Zn^{2+} and magnetic ion Fe^{3+} are distributed in A and B sites, respectively [53]. From the literatures [54–56], the bulk magnesium ferrite ($MgFe_2O_4$) has an inverse spinel structure with the preference of Mg^{2+} cations
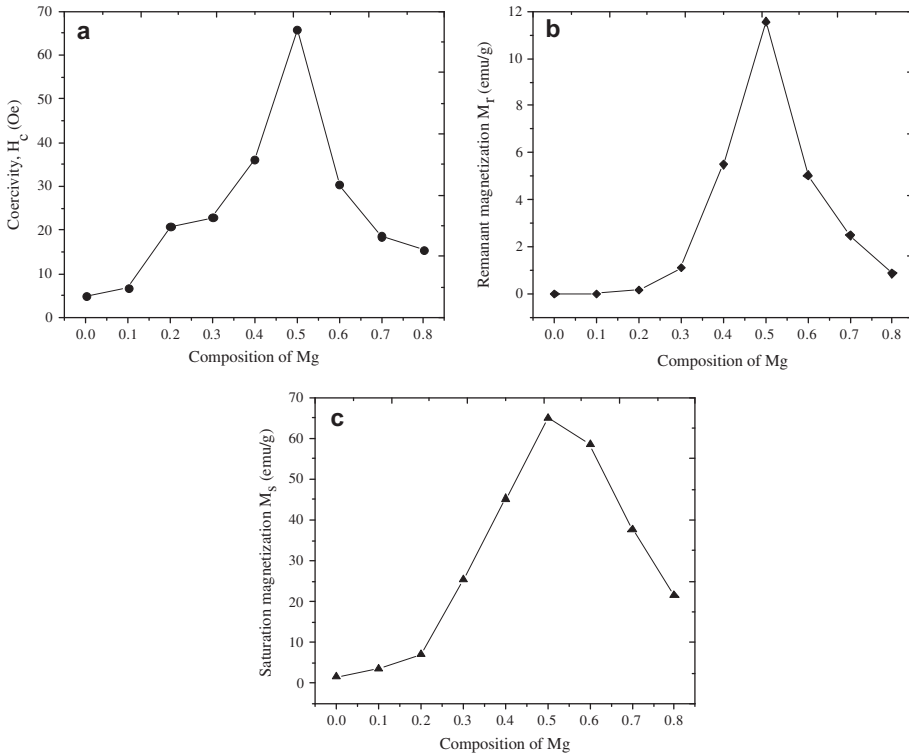
Fig. 10. VSM results of $Zn_{1-x}Mg_xFe_2O_4$ (x = 0.0, 0.1, 0.2, 0.3, 0.4, 0.5, 0.6, 0.7 and 0.8) system: (a) coercivity (H_c), (b) remanent magnetization (M_r), and (c) saturation magnetization (M_s).

Table 2
Magnetic properties (coercivity, remanent magnetization and saturation magnetization) of $Zn_{1-x}Mg_xFe_2O_4$ (x = 0.0, 0.1, 0.2, 0.3, 0.4, 0.5, 0.6, 0.7 and 0.8) system.

Samples	H_c (Oe)	M_r (emu/g)	M_s (emu/g)
$ZnFe_2O_4$	5.027	0.0016	1.638
$Zn_{0.9}Mg_{0.1}Fe_2O_4$	6.771	0.0139	3.472
$Zn_{0.8}Mg_{0.2}Fe_2O_4$	20.76	0.1754	7.121
$Zn_{0.7}Mg_{0.3}Fe_2O_4$	22.91	1.1322	25.31
$Zn_{0.6}Mg_{0.4}Fe_2O_4$	36.25	5.5041	45.16
$Zn_{0.5}Mg_{0.5}Fe_2O_4$	65.96	11.565	64.98
$Zn_{0.4}Mg_{0.6}Fe_2O_4$	30.42	5.0418	58.62
$Zn_{0.3}Mg_{0.7}Fe_2O_4$	18.63	2.4871	37.72
$Zn_{0.2}Mg_{0.8}Fe_2O_4$	15.39	0.8765	21.59

occupying the octahedral sites. Both Zn^{2+} and Mg^{2+} divalent ions are nonmagnetic in nature. The M_s of spinel ferrite nanoparticles is strongly influenced by the cationic distribution on tetrahedral and octahedral lattice sites [9]

Generally, it is believed that $ZnFe_2O_4$ should not exhibit magnetic performance as B–B superexchange interactions dominate and the B-sites magnetic moment is antiparallel to each other. However, the distribution of cation can be changed obviously, when the grain size is decreased to the nano-size. A part of Mg^{2+} may enter into B-site and Fe^{3+} enter into A-site simultaneously. As a result, the net moment is departed from zero, which attributed to the enhancement of A–B interaction. In case of

Mg-doped Zn ferrite, Zn^{2+} and Mg^{2+} ions prefer to inhabit the A- and B-sites, respectively, while Fe^{3+} prefers to inhabit both A-sites and B-sites. When the content of Mg larger is than 0.5, M_s would be decreased due to the A–B exchange interaction, which is weaker than the B–B interaction. M_s reached maximum (64.98 emu/g) when the x is 0.5, which agreed with the previous reports [9,48,57]

The ferromagnetic behavior is absent in $ZnFe_2O_4$, $Zn_{0.9}Mg_{0.1}Fe_2O_4$ and $Zn_{0.8}Mg_{0.2}Fe_2O_4$ samples, and this may be due to the non-equilibrium distribution of Fe^{3+} ions in tetrahedral and octahedral sites, which is in good agreement with previous studies [45,58–60]. The non saturation observed in MH loop, and the absence of the hysteresis, M_r and H_c indicate that the samples $ZnFe_2O_4$, $Zn_{0.9}Mg_{0.1}Fe_2O_4$ and $Zn_{0.8}Mg_{0.2}Fe_2O_4$ have superparamagnetic behavior [61,62]. Moreover, the very low value of H_c and M_r indicate that they are also soft magnets [63–66]. The lattice parameter of the samples $ZnFe_2O_4$, $Zn_{0.9}Mg_{0.1}Fe_2O_4$, $Zn_{0.8}Mg_{0.2}Fe_2O_4$, $Zn_{0.7}Mg_{0.3}Fe_2O_4$, $Zn_{0.6}Mg_{0.4}Fe_2O_4$, $Zn_{0.5}Mg_{0.5}Fe_2O_4$, $Zn_{0.4}Mg_{0.6}Fe_2O_4$, $Zn_{0.3}Mg_{0.7}Fe_2O_4$ and $Zn_{0.2}Mg_{0.8}Fe_2O_4$ decreased from 8.443 to 8.427 Å, due to the smaller ionic radius of Mg-doping (0.65 Å), leading to the contraction of the unit cell volume, which in turn decrease the inter-atomic distance between the ions, and affects the magnetic properties. Both structural and magnetic properties of Zn–Mg ferrite nanoparticles strongly depend upon Mg^{2+} cation doping percentage.

4. Conclusions

Nanocrystalline pure and Mg-doped $ZnFe_2O_4$ ($Zn_{1-x}Mg_xFe_2O_4$ with x = 0.0, 0.1, 0.2, 0.3 0.4, 0.5, 0.6, 0.7 and 0.8) samples have been successfully synthesized by a microwave combustion method using urea as the fuel, with an average particle size of 15–43 nm. The formation of cubic spinel phase was confirmed by XRD and the structural, optical and magnetic properties were analyzed. X-ray analysis confirmed the formation of the single phase for the compositions. The lattice parameter is reduced from 8.443 to 8.427 Å by increasing Mg content. UV–Visible diffuse reflectance spectroscopy shows that the energy band gap of the synthesized pure $ZnFe_2O_4$ nanoparticles is 2.15 eV and by increasing the Mg-doping, it decreases from 2.01 to 1.42 eV. In the present study, M_s and M_r increased with increasing Mg content. On doping Mg^{2+} ions, the ferromagnetic behavior increases (up to x = 0.5), which changes the shape of M–H loops. The magnetization at the maximum field monotonically increases with increasing Mg content x = 0.5, and rapidly decreased for x larger than 0.5, i.e. x = 0.6, 0.7 and 0.8, which is attributed to the change in the cationic distribution at tetrahedral and octahedral sites. Smaller values of the coercivity showed the soft magnetic nature of these $Zn_{1-x}Mg_xFe_2O_4$ nanoparticles. Thus, it can be concluded that the different changes occur in the properties of Mg doped Zn-ferrite nanoparticles is due to the rearrangements of divalent metal cations at different lattice sites.

References

[1] T. Tanaka, R. Shimazu, H. Nagai, M. Tada, T. Nakagawa, A. Sandhu, H. Handa, M. Abe, Preparation of spherical and uniform-sized ferrite nanoparticles with diameters between 50 and 150 nm for biomedical applications, J. Magn. Magn. Mater. 321 (2009) 1417–1420.

[2] M. Srivastava, A.K. Ojha, S. Chaubey, A. Materny, Synthesis and optical characterization of nanocrystalline $NiFe_2O_4$ structures, J. Alloys Compd. 481 (2009) 515–519.

[3] R. Gimenes, M.R. Baldissera, M.R.A. Silva, C.A. Silveira, D.A.W. Soares, L.A. Perazolli, M.R. Silva, M.A. Zaghete, Structural and magnetic characterization of $Mn_xZn_{1-x}Fe_2O_4$ (x = 0.2, 0.35, 0.65, 0.8, 1.0) ferrites obtained by the citrate precursor method, Ceram. Int. 38 (2012) 741–746.

[4] I. Sharifi, H. Shokrollahi, S. Amiri, Ferrite-based magnetic nanofluids used in hyperthermia applications, J. Magn. Magn. Mater. 324 (2012) 903–915.

[5] N. Gupta, A. Verma, S.C. Kashyap, D.C. Dube, Microstructural, dielectric and magnetic behavior of spin-deposited nanocrystalline nickel–zinc ferrite thin films for microwave applications, J. Magn. Magn. Mater. 308 (2007) 137–142.

[6] S. Hajarpour, K. Gheisari, A.H. Raouf, Characterization of nanocrystalline $Mg_{0.6}Zn_{0.4}Fe_2O_4$ soft ferrites synthesized by glycine–nitrate combustion process, J. Magn. Magn. Mater. 329 (2013) 165–169.

[7] A. Azam, A. Jawad, A.S. Ahmed, M. Chaman, A.H. Naqvi, Structural, optical and transport properties of Al^{3+} doped $BiFeO_3$ nano-powder synthesized by solution combustion method, J. Alloys Compd. 509 (2011) 2909–2913.

[8] A. Jawada, A.S. Ahmed, S.S.Z. Ashraf, M. Chaman, A. Azam, Exploring the dielectric behaviour of nano-structured Al^{3+} doped $BiFeO_3$ ceramics synthesized by auto ignition process, J. Alloys Compd. 530 (2012) 63–70.

[9] S. Rahman, K. Nadeem, M.A. Rehman, M. Mumtaz, S. Naeem, I.L. Papst, Structural and magnetic properties of ZnMg-ferrite nanoparticles prepared using the co-precipitation method, Ceram. Int. 39 (2013) 5235–5239.

[10] K.P. Thummer, M.C. Chhantbar, K.B. Modi, G.J. Baldha, H.H. Joshi, Localized canted spin behaviour in $Zn_xMg_{1.5-x}Mn_{0.5}FeO_4$ spinel ferrite system, J. Magn. Magn. Mater. 280 (2004) 23–30.

[11] Y. Koseoglu, A. Baykal, M.S. Toprak, F. Gozuak, A.C. Basaran, B. Aktas, Synthesis and characterization of $ZnFe_2O_4$ magnetic nanoparticles via a PEG-assisted route, J. Alloys Compd. 462 (2008) 209–213.

[12] J. Qiu, C. Wang, M. Gu, Photocatalytic properties and optical absorption of zinc ferrite nanometer films, Mater. Sci. Eng., B 112 (2004) 1–4.

[13] L. Satyanarayana, K.M. Reddy, S.V. Manorama, Synthesis of nanocrystalline $Ni_{1-x}Co_xMn_xFe_{2-x}O_4$: a material for liquefied petroleum gas sensing, Sens. Actuators, B 89 (2003) 62–67.

[14] H. Erhardt, S.J. Campbell, M. Hofman, Structural evolution of ball-milled $ZnFe_2O_4$, J. Alloys Compd. 339 (2002) 255–260.

[15] M. Sivakumar, T. Takami, H. Ikuta, A. Towata, K. Yasui, T. Tuziuti, T. Kozuka, D. Bhattacharya, Y. Iida, Fabrication of zinc ferrite nanocrystals by sonochemical emulsification and evaporation–observation of magnetization and its relaxation at low temperature, J. Phys. Chem. B 110 (2006) 15234–15243.

[16] M. Atif, S.K. Hasanain, M. Nadeem, Magnetization of sol–gel prepared zinc ferrite nanoparticles: effects of inversion and particle size, Solid State Commun. 138 (2006) 416–421.

[17] J.M. Yang, F.S. Yen, Evolution of intermediate phases in the synthesis of zinc ferrite nanopowders prepared by the tartrate precursor method, J. Alloys Compd. 450 (2008) 387–394.

[18] M. Jean, V. Nachbaur, Determination of milling parameters to obtain mechanosynthesized $ZnFe_2O_4$, J. Alloys Compd. 454 (2008) 432–436.

[19] H. Xue, Z.H. Li, X.X. Wang, X.Z. Fu, Facile synthesis of nanocrystalline zinc ferrite via a self-propagating combustion method, Mater. Lett. 61 (2007) 347–350.

[20] R.D.K. Misra, S. Gubbala, A. Kale, W.F. Egelhoff Jr., A comparison of the magnetic characteristics of nanocrystalline nickel, zinc, and manganese ferrites synthesized by reverse micelle technique, Mater. Sci. Eng., B 111 (2004) 164–174.

[21] A. Manikandan, J. Judith Vijaya, L. John Kennedy, M. Bououdina, Structural, optical and magnetic properties of $Zn_{1-x}Cu_xFe_2O_4$ nanoparticles prepared by microwave combustion method, J. Mol. Struct. 1035 (2013) 332–340.

[22] Y. Koseoglu, F. Alan, M. Tan, R. Yilgin, M. Ozturk, Low temperature hydrothermal synthesis and characterization of Mn doped cobalt ferrite nanoparticles, Ceram. Int. 38 (2012) 3625–3634.

[23] M. Sertkol, Y. Koseoglu, A. Baykal, H. Kavas, M.S. Toprak, Synthesis and magnetic characterization of $Zn_{0.7}Ni_{0.3}Fe_2O_4$ nanoparticles via microwave-assisted combustion route, J. Magn. Magn. Mater. 322 (2010) 866–871.

[24] A. Azam, Microwave assisted synthesis and characterization of Co doped Cu ferrite nanoparticles, J. Alloys Compd. 540 (2012) 145–153.

[25] Y. Koseoglu, A. Baykal, F. Gozuak, H. Kavas, Structural and magnetic properties of $Co_xZn_{1-x}Fe_2O_4$ nanocrystals synthesized by microwave method, Polyhedron 28 (2009) 2887–2892.

[26] X.Y. Li, Y. Hou, Q.D. Zhao, L.Z. Wang, A general, one-step and template-free synthesis of sphere-like zinc ferrite nanostructures with enhanced photo catalytic activity for dye degradation, J. Colloid Interf. Sci. 358 (2011) 102–108.

[27] L.M. Salah, A.M. Moustafa, I.S.A. Farag, Structural characteristics and electrical properties of copper doped manganese ferrite, Ceram. Int. 38 (2012) 5605–5611.

[28] V.K. Mittal, P. Chandramohan, B. Santanu, M.P. Srinivasan, S. Velmurugan, S.V. Narasimhan, Cation distribution in $Ni_xMg_{1-x}Fe_2O_4$ studied by XPS and mossbauer spectroscopy, Solid State Commun. 137 (2006) 6–10.

[29] F. Luo, C.H. Yan, Anti-phase boundaries pinned abnormal positive magnetoresistance in Mg doped nanocrystalline zinc spinel ferrite, Chem. Phys. Lett. 452 (2008) 296–300.

[30] A. Manikandan, J. Judith Vijaya, L. John Kennedy, M. Bououdina, Microwave combustion synthesis, structural, optical and magnetic properties of $Zn_{1-x}Sr_xFe_2O_4$ nanoparticles, Ceram. Int. 39 (2013) 5909–5917.

[31] C. Wu, W. Huang, X. Su, H. Peng, J. Wang, Y. Liu, Experimental investigation and thermodynamic calculation of the Al–Fe–P system at low phosphorus contents, CALPHAD – Comput. Coupling Phase Diagr. Thermochem. 38 (2012) 1–6.

[32] S. Klas, Y. Dubowski, G. Pritosiwi, J. Gerth, W. Calmano, O. Lahav, Extent and mechanism of metal ion incorporation into precipitated ferrites, J. Colloid Interf. Sci. 358 (2011) 129–135.

[33] K. Fitzner, Thermodynamic properties and cation distribution of the $ZnFe_2O_4$–Fe_3O_4 spinel solid solutions at 900 °C, Thermochim. Acta 31 (1979) 227–236.

[34] Q. Li, R.C. Xie, Y.W. Li, E.A. Mintz, J.K. Shang, Enhanced visible light induced photocatalytic disinfection of *E. coli* by nitrogen doped titanium oxide, Environ. Sci. Technol. 41 (2007) 5050–5056.

[35] N. Kislova, S.S. Srinivasan, Y. Emirov, E.K. Stefanakos, Optical absorption red and blue shifts in $ZnFe_2O_4$ nanoparticles, Mater. Sci. Eng. B 153 (2008) 70–77.

[36] R.B. Kale, C.D. Lokhande, Influence of air annealing on the structural, optical and electrical properties of chemically deposited CdSe nano-crystallites, Appl. Surf. Sci. 223 (2004) 343–351.

[37] C.H.B. Ng, W.Y. Fan, Shape evolution of Cu_2O nanostructures via kinetic and thermodynamic controlled growth, J. Phys. Chem. B 110 (2006) 20801–20807.

[38] B. Liu, H.C. Zeng, Salt-assisted deposition of SnO_2 on α-MoO_3 nanorods and fabrication of polycrystalline SnO_2 nanotubes, J. Phys. Chem. B 108 (2004) 5867–5874.

[39] A.V. Dijken, E.A. Meulenkamp, D. Vanmaekelbergh, A. Meijerink, Identification of the transition responsible for the visible emission in ZnO using quantum size effects, J. Lumin. 90 (2000) 123–128.

[40] D. Gao, Z. Shi, Y. Xu, J. Zhang, G. Yang, J. Zhang, X. Wang, D. Xue, Synthesis, magnetic anisotropy and optical properties of preferred oriented zinc ferrite nanowire arrays, Nanoscale Res. Lett. 5 (2010) 1289–1294.

[41] P.H. Borse, J.S. Jang, S.J. Hongand, J.S. Lee, J.H. Jung, T.E. Hong, C.W. Ahn, E.D. Jeong, K.S. Hong, J.H. Yoon, H.G. Kim, Photocatalytic hydrogen generation from water–methanol mixtures using nanocrystalline $ZnFe_2O_4$ under visible light irradiation, J. Korean Phys. Soc. 55 (4) (2009) 1472–1477.

[42] G. Fan, Z. Gu, L. Yang, F. Li, Nanocrystalline zinc ferrite photocatalysts formed using the colloid mill and hydrothermal technique, Chem. Eng. J. 155 (2009) 534–541.

[43] P.P. Hankare, R.S. Pandav, R.P. Patil, V.T. Vader, K.M. Garadkar, Synthesis, structural and magnetic properties of copper substituted nickel manganite, J. Alloys Compd. 544 (2012) 197–202.

[44] P.P. Hankare, K.R. Sanadi, K.M. Garadkar, D.R. Patil, I.S. Mulla, Synthesis and characterization of nickel substituted cobalt ferrite nanoparticles by sol–gel auto-combustion method, J. Alloys Compd. 553 (2013) 383–388.

[45] S. Ayyappan, S.P. Raja, C. Venkateswaran, J. Philip, B. Raj, Room temperature ferromagnetism in vacuum annealed $ZnFe_2O_4$ nanoparticles, Appl. Phys. Lett. 96 (2010) 143106.
[46] G.F. Goya, H.R. Rechenberg, Ionic disorder and Neel temperature in $ZnFe_2O_4$ nanoparticles, J. Magn. Magn. Mater. 196–197 (1999) 191–192.
[47] A. Goldman, Modern Ferrite Technology, second ed., Springer, New York, NY, USA, 2006.
[48] H. Wu, N. Zhang, L. Mao, T. Li, L. Xia, Controlled synthesis and magnetic properties of monodisperse $Ni_{1-x}Zn_xFe_2O_4$/MWCNT nanocomposites via microwave-assisted polyol process, J. Alloys Compd. 554 (2013) 132–137.
[49] H. Sozeri, Z. Durmus, A. Baykal, Structural and magnetic properties of triethylene glycol stabilized $Zn_xCo_{1-x}Fe_2O_4$ nanoparticles, Mater. Res. Bull. 47 (2012) 2442–2448.
[50] P. Yadoji, R. Peelamedu, D. Agrawal, R. Roy, Microwave sintering of Ni–Zn ferrites: comparison with conventional sintering, Mater. Sci. Eng. B 98 (2003) 269–278.
[51] P.P. Sarangi, S.R. Vadera, M.K. Patra, N.N. Ghosh, Synthesis and characterization of pure single phase Ni–Zn ferrite nanopowders by oxalate based precursor method, Powder Technol. 203 (2010) 348–353.
[52] M.A. Gabal, Reda M. El-Shishtawy, Y.M. Al Angari, Structural and magnetic properties of nano-crystalline Ni–Zn ferrites synthesized using egg-white precursor, J. Magn. Magn. Mater. 324 (2012) 2258–2264.
[53] K.P. Thummer, M.C. Chhantbar, K.B. Modi, G.J. Baldha, H.H. Joshi, Localized canted spin behaviour in $Zn_xMg_{1.5-x}Mn_{0.5}Fe_2O_4$ spinel ferrite system, J. Magn. Magn. Mater. 280 (2004) 23–30.
[54] A. Pradeep, P. Priyadharsini, G. Chandrasekaran, Sol–gel route of synthesis of nanoparticles of $MgFe_2O_4$ and XRD, FTIR and VSM study, J. Magn. Magn. Mater. 320 (2008) 2774–2779.
[55] V. Sepelak, D. Baabe, D. Mienert, F.J. Litterst, K.D. Becker, Enhanced magnetisation in nanocrystalline high-energy milled $MgFe_2O_4$, Scripta Mater. 48 (2003) 961–966.
[56] Y. Ichiyanagi, M. Kubota, S. Moritake, Y. Kanazawa, T. Yamada, T. Uehashi, Magnetic properties of Mg-ferrite nanoparticles, J. Magn. Magn. Mater. 310 (2007) 2378–2380.
[57] M.M. Rashad, E.M. Elsayed, M.M. Moharam, R.M.A. Shahba, A.E. Saba, Structure and magnetic properties of $Ni_xZn_{1-x}Fe_2O_4$ nanoparticles prepared through co-precipitation method, J. Alloys Compd. 486 (2009) 759–767.
[58] M. Bohra, S. Prasad, N. Kumar, D.S. Misra, S.C. Sahoo, N. Venkataramani, R. Krishnan, Large room temperature magnetization in nanocrystalline zinc ferrite thin films, Appl. Phys. Lett. 88 (2006) 262506.
[59] S. Nakashima, K. Fujita, K. Tanaka, K. Hirao, T. Yamamoto, I. Tanaka, Thermal annealing effect on magnetism and cation distribution in disordered $ZnFe_2O_4$ thin films deposited on glass substrates, J. Magn. Magn. Mater. 310 (2007) 2543–2545.
[60] Y. Changwa, Z. Qiaoshi, G.F. Goya, T. Torres, L. Jinfang, W. Haiping, G. Mingyuan, Z. Yuewu, W. Youwen, J.Z. Jiang, $ZnFe_2O_4$ nanocrystals: synthesis and magnetic properties, J. Phys. Chem. C 111 (2007) 12274–12278.
[61] O.M. Lemine, M. Bououdina, M. Sajieddine, A.M. Al-Saie, M. Shafi, A. Khatab, M. Alhilali, M. Henini, Synthesis, structural, magnetic and optical properties of nanocrystalline $ZnFe_2O_4$, Physica B 406 (2011) 1989–1994.
[62] Y. Koseoglu, Structural, magnetic, electrical and dielectric properties of $Mn_xNi_{1-x}Fe_2O_4$ spinel nanoferrites prepared by PEG assisted hydrothermal method, Ceram. Int. 39 (2013) 4221–4230.
[63] P.P. Hankare, R.P. Patil, A.V. Jadhav, K.M. Garadkar, R. Sasikala, Enhanced photocatalytic degradation of methyl red and thymol blue using titania–alumina–zinc ferrite nanocomposite, Appl. Catal B: Environ. 107 (2011) 333–339.
[64] A.E. Berkowitz, R.H. Kodama, S.A. Makhlouf, F.T. Parker, F.E. Spada, E.J. McNiff Jr., S. Foner, Anomalous properties of magnetic nanoparticles, J. Magn. Magn. Mater. 196–197 (1999) 591–594.
[65] V. Sepelak, L. Wilde, U. Steinike, K.D. Becker, Thermal stability of the non-equilibrium cation distribution in nanocrystalline high-energy milled spinel ferrite, Mater. Sci. Eng. A 865 (2004) 375–377.
[66] P.P. Hankare, K.R. Sanadi, R.S. Pandav, N.M. Patil, K.M. Garadkar, I.S. Mulla, Structural, electrical and magnetic properties of cadmium substituted copper ferrite by sol–gel method, J. Alloys Compd. 540 (2012) 290–296.